




Ferromagnetic metallic Sr-rich $\text{Ln}_{1/2}\text{A}_{1/2}\text{CoO}_3$ cobaltites with spontaneous spin rotation

Jessica Padilla-Pantoja ¹, Arnau Romaguera,¹ Xiaodong Zhang,¹ Javier Herrero-Martín ², Francois Fauth,² Javier Blasco,³ and José Luis García-Muñoz ^{1,*}

¹*Institut de Ciència de Materials de Barcelona, ICMA-B-CSIC, Campus UAB, 08193 Bellaterra, Spain*

²*CELLS-ALBA Synchrotron, 08290 Cerdanyola del Vallès, Catalunya, Spain*

³*Instituto de Nanociencia y Materiales de Aragón, Departamento de Física de la Materia Condensada, CSIC-Universidad de Zaragoza, C/ Pedro Cerbuna 12, 50009 Zaragoza, Spain*



(Received 9 March 2021; revised 14 July 2021; accepted 14 July 2021; published 9 August 2021)

The $\text{Pr}_{0.50}\text{Sr}_{0.50}\text{CoO}_3$ perovskite exhibits unique magnetostructural properties among the rest of ferromagnetic (FM)/metallic $\text{Ln}_{0.50}\text{Sr}_{0.50}\text{CoO}_3$ compounds. The sudden orthorhombic-tetragonal ($Imma \rightarrow I4/mcm$) structural transition produces an unusual magnetic behavior vs temperature and external magnetic fields. The symmetry change is responsible for a spontaneous spin rotation in this metallic oxide. We have studied half-doped $\text{Ln}_{0.50}(\text{Sr}_{1-x}\text{A}_x)_{0.50}\text{CoO}_3$ cobaltites varying the ionic radius r_A of A -site cations (divalent cations and lanthanides) to complete the T - r_A phase diagram. The influence of the structural distortion and the A -cation size for the occurrence of a spontaneous spin reorientation in the metallic state has been investigated. As the magnetization reorientation is driven by the temperature-induced collapse of the orthorhombic distortion, a careful investigation of the structural symmetry is presented, varying the structural distortion of the Sr-rich half-doped cobaltites by means of both compositional and temperature changes. The region in the phase diagram of these FM/metallic cobaltites where $Fm'm'm$ magnetic symmetry replaces $Im'm'a$ was determined. In that region, the magnetization direction has rotated 45° within the a - b plane from the former to the latter.

DOI: [10.1103/PhysRevB.104.054411](https://doi.org/10.1103/PhysRevB.104.054411)

I. INTRODUCTION

Cobalt oxides attract much attention, as they present a rich variety of interesting phenomena. Among other remarkable properties, cobalt compounds are well suited for applications as mixed conductors, materials for solid oxide fuel cells, thermopower applications, room temperature (RT) ferromagnets, superconductivity, magnetoelectric materials, high temperature solar absorbers, or materials for spintronics [1–6]. Moreover, the ability of cobalt oxides containing Co^{3+} ions to adopt different spin states is a relevant feature due to the importance of the spin state of Co for electron mobility, the nature of magnetic coupling, or the structural stability. The perovskite-type cobaltites LnCoO_3 , $\text{Ln}_{1-x}\text{Ca}_x\text{CoO}_3$, and $\text{LnBaCo}_2\text{O}_{5+d}$ (Ln = lanthanide) are good examples of systems exhibiting phase transitions triggered by spin-state changes [7–11]. Examples of both ferromagnetic (FM) metals and insulators (of great potential for spintronic applications) are found among the rich ecosystem of cobalt oxides [6].

The double-exchange interaction (as in the widely studied manganites) exemplifies an effective mechanism to produce FM metallic states in many cobaltites. The hybridization between $3d$ metal and $2p$ oxygen orbitals is more intense in cobalt oxides than in manganites favoring the delocalization of charges. Referent examples are the half-doped $\text{Pr}_{0.50}\text{A}_{0.50}\text{CoO}_3$ ($A = \text{Ca}, \text{Sr}, \text{or Ba}$) compounds, where Co^{3+} and Co^{4+} species coexist in a 1:1 ratio. Despite sharing a

metallic behavior, their properties and structure strongly differ.

(i) $\text{PrBaCo}_2\text{O}_6$ was assigned to the $P4/mmm$ space group (SG) with ordered double perovskite structure, where Pr and Ba form alternating layers along the c axis [12]. This “112” layered cobaltite presents a Curie temperature $T_C = 210$ K in virtue of the double-exchange mechanism.

(ii) The half-doped cobaltite $\text{Pr}_{0.50}\text{Ca}_{0.50}\text{CoO}_3$ (PCCO) is metallic but undergoes a metal-insulator transition (MIT) upon cooling at $T_{\text{MI}} \approx 80$ K, becoming insulating [7]. Its $Pnma$ crystal symmetry is preserved across the MIT [13]. This Ca compound does not exhibit spontaneous magnetic order, but an exceptional electronic mechanism based on the stabilization of the Co^{3+} LS (low-spin) state at T_{MI} . A spin-state change in a fraction of cobalt atoms is concurrent at T_{MI} with a sudden partial Pr^{3+} to Pr^{4+} valence change. Consequently, at the MIT, there is a transfer of electrons from Pr to Co sites [14–16]. $\text{Pr}_{0.50}\text{Ca}_{0.50}\text{CoO}_3$ attracts interest in ultrafast optical switching devices due to its proven ability of generating metallic domains in the insulating low-temperature phase by ultrafast photoexcitation [17–20].

(iii) The MIT seen in PCCO does not take place in $\text{Pr}_{0.50}\text{Sr}_{0.50}\text{CoO}_3$ (PSCO). The compound doped with Sr presents a (less distorted) $Imma$ structure [21,22], where the partial Pr^{3+} to Pr^{4+} valence shift and Co spin-state transition of PCCO are found suppressed [23]. Instead, Mahendiran and Schiffer [24] reported unexpected magnetic anomalies at $T_{\text{SR}} \approx 120$ K, well below the FM transition at $T_C \approx 230$ K. A reorientation of the magnetization axis was suggested by Lorentz transmission electron microscopy (LTEM) images by

*Corresponding author: garcia.munoz@icmab.es

Uchida *et al.* [25] and by means of x-ray magnetic circular dichroism experiments [26,27], and confirmed by neutron diffraction data and symmetry analyses [28]. A rotation of the magnetization axis by 45° within the a - b plane takes place spontaneously in PSCO across the second magnetic transition observed in the magnetization curves. This Sr-rich perovskite retains its metallic character across the unexpected magnetostructural transition at T_{SR} .

The discovery of materials presenting spin-rotation (SR) transitions attracts substantial attention within the condensed matter physics community. From a basic physics point of view, it is of great interest to recognize the microscopic origin of these transitions for a better understanding of order and dynamic phenomena in classical and quantum magnets. In applied fields developing nanocomponents for spintronic devices, such as spin-torques, the possibility of using spins instead of charges as the variable state for computation or operation demands manipulating the spin orientation of nanomagnets to switch between logic or conductive states [29,30]. SRs can be also used for the optical control of magnetically ordered materials. For instance, because of laser-induced heating and a subsequent spin reorientation phase transition, ultrafast excitations of quasi-FM modes have been reported for canted antiferromagnets such as some $LnFeO_3$ oxides [31].

Given the increasing importance of FM oxides presenting SR transitions, in this paper, we investigate the stability of the SR transition reported for the compound PSCO with respect to the distortion of the perovskite structure in the family of half-doped Sr-rich $Ln_{0.50}A_{0.50}CoO_3$ cobaltites.

II. EXPERIMENTAL DETAILS

Half-doped cobaltites $Ln_{0.50}A_{0.50}CoO_3$ with compositions relatively close to the reference compound PSCO were prepared by solid-state reaction or sol-gel methods. First, $Ln_{0.50}Sr_{0.50}CoO_3$ perovskites with $Ln = Pr, Pr_{0.95}Tb_{0.05}, Nd,$ and Tb were prepared by solid-state reaction at high temperature under oxygen atmosphere. High-purity $Co_3O_4, Pr_6O_{11},$ and corresponding Ln_2O_3 oxides were first dried at $1100^\circ C$. $SrCO_3$ was heated at $850^\circ C$, then up to $950^\circ C$ to achieve decarbonation. The precursors were then mixed up, pressed into pellets, and heated in oxygen atmosphere at $1000^\circ C$ for 12 h, with a slow cooling. After gridding and pressing, the annealing procedure was repeated several times, the last one being performed at $1170^\circ C$ (during 24 h) under O_2 flow, followed by a slow cooling ($60^\circ C/h$). Secondly, several compositions of the type $Pr_{0.50}(Sr_{1-x}Ca_x)CoO_3$ (with $0.025 \leq x \leq 0.10$) were also prepared following a similar procedure but adding $CaCO_3$. In addition, a bigger alkaline-earth ion was used in the mixed half-doped cobaltites $Pr_{0.50}(Sr_{1-x}Ba_x)_{0.50}CoO_3$, where the Sr^{2+} ion was progressively substituted by the bigger Ba^{2+} . Applying a sol-gel synthesis method (instead of the solid-state reaction) allowed us to extend the Ba doping range before the appearance of secondary phases. $Pr_{0.50}(Sr_{1-x}Ba_x)_{0.50}CoO_3$ samples with $x = 0.025, 0.05,$ and 0.10 were thus prepared by sol-gel using stoichiometric amounts of Pr_6O_{11}, Co -metal, $SrCoO_3,$ and $BaCoO_3$. The mixture of reactives was dissolved in a solution of HNO_3 1M, by adding citric acid and ethylene

glycol. The pink solution was slowly evaporated, leading to a brown resin which was first dried at $650^\circ C$ for 6 h. The obtained precursor was pressed into pellets and heated under O_2 atmosphere during several annealing cycles in the range of 1175 – $1200^\circ C$, with intermediate grindings and pressings. The final product was heated again at $800^\circ C$ for 16 h under the same atmosphere (O_2) and cooled slowly ($60^\circ C/h$).

X-ray diffraction patterns were recorded at RT using a Siemens D-5000 diffractometer and $Cu K\alpha$ radiation. Electrical transport (using the four-probe method) and magnetization measurements were performed using a Physical Properties Measuring System and a superconducting quantum interferometer device from Quantum Design. Our preliminary characterization confirmed well-crystallized and single-phased perovskites.

Neutron diffraction measurements were carried out at the high-flux reactor of the Institut Laue Langevin (Grenoble, France) using the high-intensity D20 ($\lambda = 1.594 \text{ \AA}, 1.87 \text{ \AA}$), D1B ($\lambda = 2.52 \text{ \AA}$) and the high-resolution D2B ($\lambda = 1.594 \text{ \AA}$) diffractometers. Vanadium cylinder sample holders were loaded with ~ 10 g of powder sample. Neutron powder diffraction (NPD) patterns of several compositions were recorded at variable temperatures using helium cryostats and a cryofurnace, within the 10 – 450 K temperature range. Moreover, synchrotron x-ray powder diffraction (SXRPD) measurements were performed in the BL04-MSPD beamline [32] of the ALBA Synchrotron Light Facility (Barcelona, Spain) using a wavelength $\lambda = 0.41290(3) \text{ \AA}$, which was determined by measuring a National Institute of Standards and Technology standard silicon. The samples were loaded in borosilicate glass capillaries (0.5 - and 0.7 -mm diameter) and kept spinning during data acquisition. For selected compositions, patterns between 10 and 300 K were collected using a Dynaflo liquid He cryostat. Two detection systems, the MAD detection setup (13-channel multianalyzer detector) and the position-sensitive detector MYTHEN, were used. Structural and magnetic Rietveld refinements were carried out using the FULLPROF program [33]. Neutron refinement of the oxygen occupation factors did not detect oxygen vacancies within an estimated error of $\sim 3\%$. Variable oxygen occupancies did not improve the agreement factors in the neutron fits.

III. RESULTS AND DISCUSSION

A. Half-doped Sr-rich cobaltites with spontaneous SR

1. $Pr_{0.50}Sr_{0.50}CoO_3$

The structural and magnetic properties of the PSCO sample used in this paper have been exhaustively described in Refs. [21,22,28]. In these previous reports, the successive structural and magnetic phases were investigated and comprehensively described as a function of temperature (T). Figure 1 shows the magnetization of the PSCO sample [after field cooling (FC)] under 10 Oe and 1 kOe. Concurrent with the spin reorientation, at 120 K, there is a loss/gain of magnetization, depending on the value of the applied field: $H < H_{cr}$ or $H > H_{cr}$, respectively (critical field $H_{cr} \approx 300$ Oe). In the following, the distinct FM phases below and above the

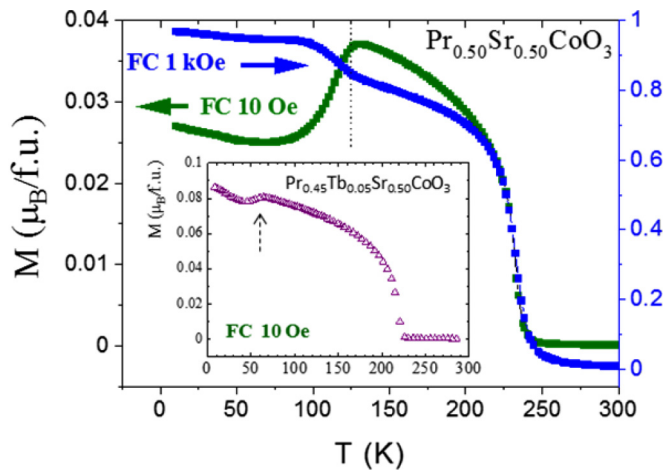


FIG. 1. Field-cooled $M(T)$ curves for PSCO showing negative and positive steps under 10 Oe and 1 kOe, respectively. The spin rotation (SR) transition is indicated by a dotted line. Inset: Field cooling (FC) $M(T)$ for $\text{Pr}_{0.45}\text{Tb}_{0.05}\text{Sr}_{0.50}\text{CoO}_3$ (10 Oe), where we found $T_C \approx 224$ K and $T_{\text{SR}} \approx 60$ K.

transition at $T_{\text{SR}} \approx 120$ K will be, respectively, named FM1 and FM2. Both the orbital and spin components of the collinear Co moments rotate by 45° across the transition [28].

Upon cooling from high temperatures, PSCO exhibits the following succession of phase transformations: $Pm\text{-}3m \rightarrow R\text{-}3c \rightarrow Imma \rightarrow I4/mcm$, all keeping the metallic state. The corresponding transition temperatures can be labeled as T_{CR} , T_{RO} , and T_{OT} , respectively. In the Glazer notation [34], the chain of changes between successive tilt systems (referred to the pseudocubic axes) can be easily visualized as $a^0a^0a^0 \rightarrow a^-a^-a^- \rightarrow a^-a^-c^0 \rightarrow a^0a^0c^-$ [21]. The two last transitions (at $T_{\text{RO}} = 314$ K and $T_{\text{OT}} = T_{\text{SR}} = 120$ K) are shown in Fig. 2(a), where we plot a projection of the thermal evolution of the neutron diffracted intensities (adapted from Ref. [21]). A comparison of the orthorhombic (O) and tetragonal (T) phases can be found in Ref. [21], where selected interatomic distances and bond angles were also reported for the $Imma$ (O) and $I4/mcm$ (T) structures refined at 300 and 15 K.

The characteristics of the FM1 and FM2 phases were deduced by analyses of the NPD data, and their respective magnetic SGs (MSG) were also determined by García-Muñoz *et al.* [28]. PSCO orders below the Curie point ($T_C = 230$ K) with the FM moments parallel to the a axis in the $Imma$ cell ($F_x, \sqrt{2}a_0 \times 2a_0 \times \sqrt{2}a_0$). We name this phase FM2, and its MSG is $Im'm'a$ [Nr. 74.558, transformation to standard setting: (a, b, c; 0, 0, 0)]. At 140 K, the refined FM moment was $m_x = 1.49(3) \mu_B/\text{Co}$ [28]. At 120 K, the compound adopts the FM1 phase (SR) through a $Im'm'a \rightarrow Fm'm'm$ phase transition involving new structural and magnetic symmetries. As for the magnetic symmetry in the $I4/mcm$ tetragonal phase ($\sqrt{2}a_0 \times \sqrt{2}a_0 \times 2a_0$ cell), we found the $Fm'm'm$ magnetic SG [Nr. 69.524, transformation to standard setting: (-c, a-b, -a-b; 0, $\frac{1}{2}$, 0)] with Co moments within the a - b plane and $m_x = m_y = 1.32(3) \mu_B/\text{atom}$ at 15 K (F_{xy} or diagonal

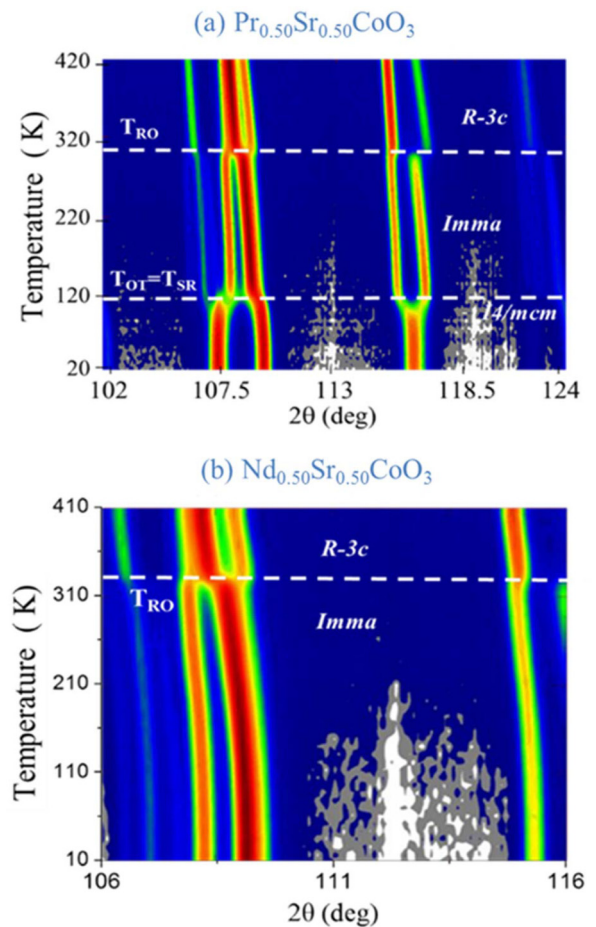


FIG. 2. Neutron diffraction intensities for characteristic reflections of the successive crystal structures as a function of temperature (D20, $\lambda = 1.87$ Å) for (a) $\text{Pr}_{0.50}\text{Sr}_{0.50}\text{CoO}_3$ (adapted from Ref. [21]) and (b) $\text{Nd}_{0.50}\text{Sr}_{0.50}\text{CoO}_3$. Notice the absence of the tetragonal phase in the Nd compound.

ferromagnetism). This description nicely accounts for both the NPD and LTEM results [25,28].

2. Probing the SR in half-doped

$\text{Pr}_{0.50}(\text{Sr}_{1-x}\text{A}_x)_{0.50}\text{CoO}_3$ ($A = \text{Ba}$ or Ca)

The evolution of the properties observed in PSCO upon varying the average distortion of the perovskite structure was first investigated by means of magnetization measurements. These were performed on two main sets of samples: $\text{Pr}_{0.50}(\text{Sr}_{1-x}\text{A}_x)_{0.50}\text{CoO}_3$ with (a) $A = \text{Ca}$ to reduce the ionic radius at the A site, and (b) with $A = \text{Ba}$ to increase the average radius r_A and decrease the distortion of the perovskite structure. Magnetization and resistivity measurements bear out that all the compositions studied are FM and metallic. Figure 3 shows the magnetization $M(T)$ of the samples with Ca content $x = 0, 0.025, 0.05, 0.075$, and 0.10 as measured under FC (10 Oe). The two magnetic transitions are evident as they produce abrupt changes in the curves at T_C (PM-FM2) and T_{SR} (FM2-FM1) for $x = 0, 0.025$, and 0.05 samples. A single transition (at T_C) is observed in the highest Ca-doped compositions $x = 0.075$ and 0.10, therefore indicating the disappearance of the magnetostructural transition. The

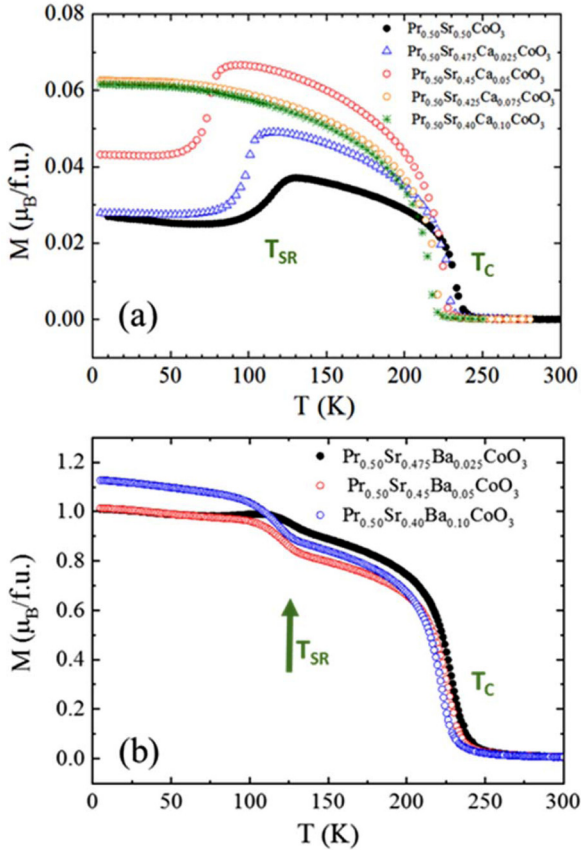


FIG. 3. Magnetization [field cooling (FC)] for (a) $\text{Pr}_{0.50}(\text{Sr}_{1-x}\text{Ca}_x)_{0.50}\text{CoO}_3$ ($x = 0, 0.025, 0.05, 0.075, \text{ and } 0.10$; 10 Oe) and (b) $\text{Pr}_{0.50}(\text{Sr}_{1-x}\text{Ba}_x)_{0.50}\text{CoO}_3$ samples with Ba contents $x = 0.025, 0.05, \text{ and } 0.10$ (1 kOe). The steplike anomaly in $M(T)$ discloses the occurrence of the 45° spin rotation (SR) of Co moments driven by the O-T symmetry change at T_{SR} . The SR anomaly is not present in Ca-7.5% and Ca-10% doped samples.

corresponding T_C and T_{SR} transition temperatures for all the compositions doped with Ca can be seen in Table I. The presence of Ca produces a gradual decrease of the T_{SR} values, and the vanishing of this transition in the range $x \approx 6\text{--}7\%$ Ca. A smoother decrease is observed for T_C when substituting Sr with Ca. Table I also shows the coercivity and remnant

magnetization measured at 10 K, which were obtained from magnetic hysteresis loops collected with a maximum applied field of 70 kOe. Figure S1 (Supplemental Material [35]) shows the magnetic hysteresis cycles for the different compositions. The remnant magnetization is very similar, but there is a smooth decrease in the coercivity by increasing the Ca content accompanied by a sudden, marked drop in the H_c values for $x > 0.07$. This agrees with the results mentioned above for the Ca series, and it indicates that the FM ground state for the compositions with $x \geq 0.075$ is different (FM2) to the tetragonal FM phase (FM1) of the samples with $x < 0.075$. For the latter, the evolution of the amplitude and sign of the magnetization jumps with the applied field is shown in Fig. 4 (samples with $x = 0$ and 0.05).

In addition to the decrease of the FM2-FM1 (spin-reorientation) transition temperature (T_{SR}), Fig. 4 shows an ostensible decrease in the critical field H_{cr} , from $H_{\text{cr}} \approx 300$ Oe (for $x = 0$) to $H_{\text{cr}} \approx 150$ Oe (for $x = 0.05$). Here, H_{cr} defines the crossover from negative to positive ΔM values at T_{SR} . The loss of magnetization (negative step) under low fields ($H < H_{\text{cr}}$) is due to the presence of conjugated [110] and [1-10] magnetic domains below the $Imma \rightarrow I4/mcm$ transition. Thus, H_{cr} is related to the magnetic anisotropy within the a - b plane.

An independent confirmation of the suppression of the O-T structural transition in the samples with $x[\text{Ca}] > 0.07$ was obtained by synchrotron diffraction on $\text{Pr}_{0.50}\text{Sr}_{0.40}\text{Ca}_{0.10}\text{CoO}_3$. This composition was found to adopt the orthorhombic $Imma$ phase, without structural changes under cooling. We confirmed that this symmetry persists down to low temperatures, without being substituted by the tetragonal structure. Figure 5 shows the synchrotron diffraction pattern collected at 10 K for $\text{Pr}_{0.50}\text{Sr}_{0.40}\text{Ca}_{0.10}\text{CoO}_3$, satisfactorily refined using the $Imma$ symmetry. Its detailed structure is reported in Table II as refined at 10 K. Therefore, the ground magnetic state of this sample corresponds to the FM orthorhombic phase FM2. This contrasts with $\text{Pr}_{0.50}\text{Sr}_{0.45}\text{Ca}_{0.05}\text{CoO}_3$, which exhibits a SR at $T_{\text{SR}} \approx 79$ K and the tetragonal FM1 ground state.

Next, we will present the main results obtained when, instead of smaller Ca^{2+} ions, larger Ba^{2+} are partially replacing Sr^{2+} sites. Single-phased well-crystallized samples of the $\text{Pr}_{0.50}(\text{Sr}_{1-x}\text{Ba}_x)_{0.50}\text{CoO}_3$ series were obtained for up

TABLE I. Transition temperatures and magnetic properties as obtained from magnetization measurements. The coercive fields (H_c) and remnant magnetization (M_r) values were obtained from magnetic hysteresis loops recorded at 10 K.

Sample	Low- T structure	T_C (K)	T_{SR} (K)	M_r ($\mu_B/\text{f.u.}$)	H_c (Oe)
$\text{Pr}_{0.50}\text{Sr}_{0.50}\text{CoO}_3$	$I4/mcm$	236	124	0.605(4)	466(2)
$\text{Pr}_{0.50}\text{Sr}_{0.475}\text{Ba}_{0.025}\text{CoO}_3$	$I4/mcm$	235	129	0.596(4)	395(2)
$\text{Pr}_{0.50}\text{Sr}_{0.45}\text{Ba}_{0.05}\text{CoO}_3$	$I4/mcm$	231	128	0.594(4)	390(2)
$\text{Pr}_{0.50}\text{Sr}_{0.40}\text{Ba}_{0.10}\text{CoO}_3$	$I4/mcm$	226	126	0.597(4)	160(2)
$\text{Pr}_{0.50}\text{Sr}_{0.475}\text{Ca}_{0.025}\text{CoO}_3$	$I4/mcm$	229	100	0.614(4)	381(2)
$\text{Pr}_{0.50}\text{Sr}_{0.45}\text{Ca}_{0.05}\text{CoO}_3$	$I4/mcm$	227	79	0.677(4)	377(2)
$\text{Pr}_{0.45}\text{Tb}_{0.05}\text{Sr}_{0.50}\text{CoO}_3$	$I4/mcm$	224	60	0.907(4)	483(2)
$\text{Nd}_{0.50}\text{Sr}_{0.50}\text{CoO}_3$	$Imma$	225	–	0.651(4)	1750(3)
$\text{Pr}_{0.50}\text{Sr}_{0.425}\text{Ca}_{0.075}\text{CoO}_3$	$Imma$	221	–	0.652(4)	842(2)
$\text{Pr}_{0.50}\text{Sr}_{0.40}\text{Ca}_{0.10}\text{CoO}_3$	$Imma$	217	–	0.598(4)	844(2)
$\text{Tb}_{0.50}\text{Sr}_{0.50}\text{CoO}_3$	$Imma$	120	–	1.599(5)	1832(5)

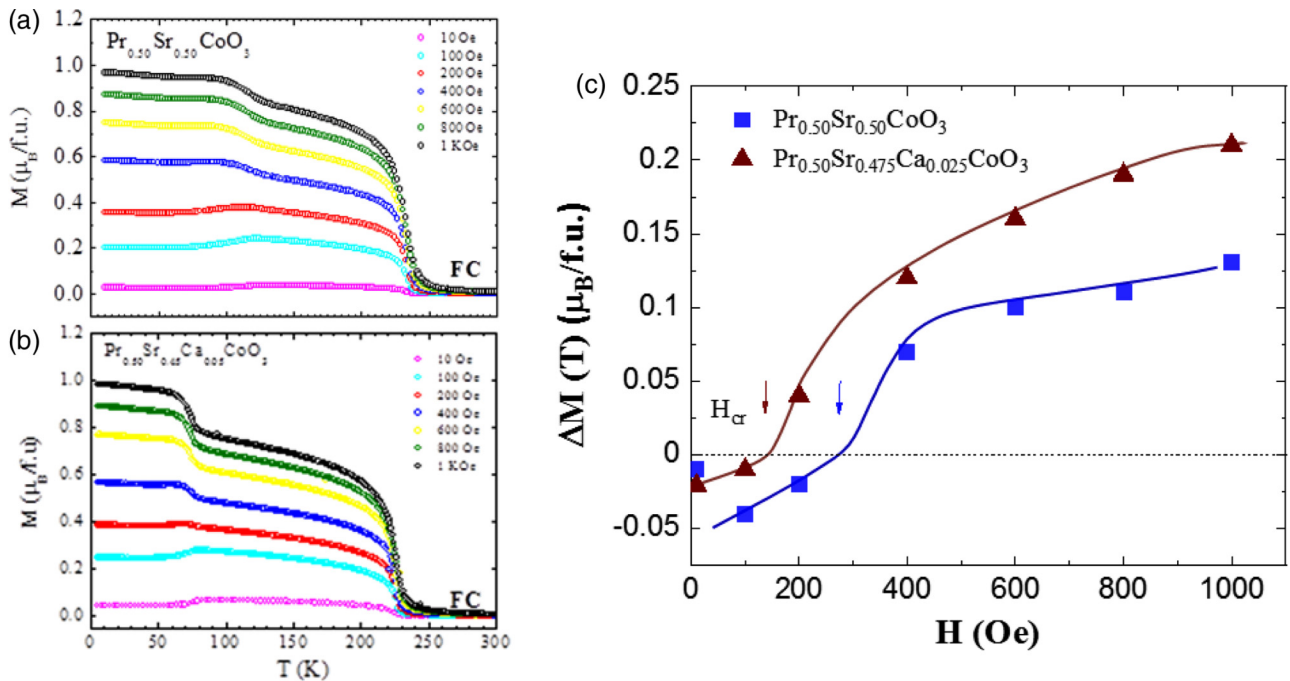


FIG. 4. (left) Magnetization $M(T)$ measured at different fields [H : 10, 100, 200, 400, 600, 800, and 1000 Oe, field cooling (FC)] in $\text{Pr}_{0.5}\text{Sr}_{0.5-x}\text{Ca}_x\text{CoO}_3$. Comparison for (a) $x = 0$ and (b) $x = 0.05$ samples. The sign of the magnetization jumps at T_{SR} is field dependent. (right) (c) Amplitude and sign of the magnetization jumps at the spin-rotation (SR) transition ($T_{\text{SR}} = T_{\text{OT}}$) as a function of the applied magnetic field. The field H_c for the crossover from negative to positive magnetization steps ΔM decreases from $H_c \approx 300$ Oe ($x = 0$) to 150 Oe ($x = 5\%$ Ca).

to a 10% substitution rate (samples with higher Ba content presented secondary phases). Their x-ray diffraction patterns were well reproduced by the $Imma$ SG. Figure 3(b) displays the T evolution of the magnetization for three $\text{Pr}_{0.5}(\text{Sr}_{1-x}\text{Ba}_x)_{0.5}\text{CoO}_3$ compositions with increasing Ba content ($x[\text{Ba}] = 0.025, 0.05, \text{ and } 0.10$). One can see that all these compositions exhibit the characteristic anomaly in $M(T)$ produced by the occurrence of the O-T symmetry change and the reorientation of the magnetization (T_{SR}). T_{SR} and T_C values obtained for Ba-doped samples are also given in Table I. In the same way the coercive field and remnant magnetization extracted from hysteresis loops (see Fig. S1 in the supplemental information) are summarized in Table I. As expected, they

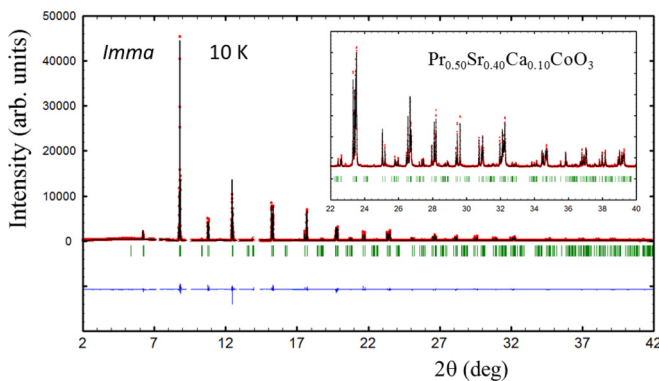


FIG. 5. $\text{Pr}_{0.5}\text{Sr}_{0.40}\text{Ca}_{0.10}\text{CoO}_3$: Rietveld refinement (black line) of the synchrotron x-ray pattern at 10 K using the $Imma$ space group (SG; MSPD; red circles, experimental points; bottom blue line, difference). Inset: Detail of the high-angles region.

are like the values found in the rest of studied compositions where we have confirmed a low- T $I4/mcm$ structure. We find that the coercivity in the ground state is systematically higher in the specimens keeping the $Imma$ symmetry.

The phase transitions in $\text{Pr}_{0.5}\text{Sr}_{0.40}\text{Ba}_{0.10}\text{CoO}_3$ were further investigated by synchrotron and neutron diffraction. This is the Ba-doped Sr-based cobaltite with the largest cell (and lowest distortion) among the ones we synthesized. Diffraction data were collected within the 2–300 K range. Figure 6 displays a projection of the thermal evolution of the synchrotron x-ray diffracted intensities in selected angular intervals. One can see the O-T structural transition (T_{OT})

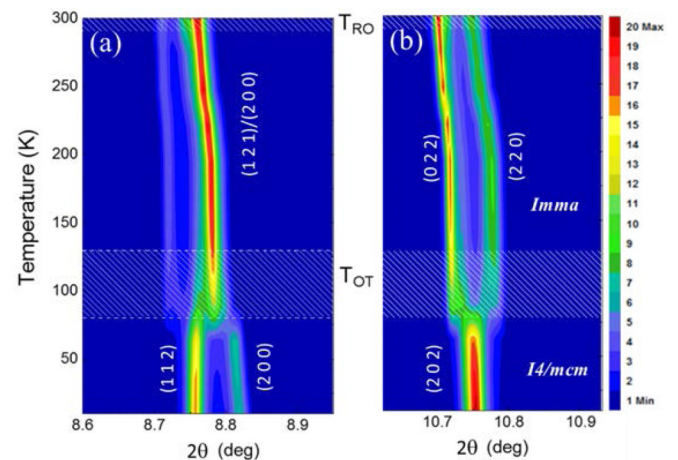


FIG. 6. $\text{Pr}_{0.5}\text{Sr}_{0.40}\text{Ba}_{0.10}\text{CoO}_3$: evolution of the synchrotron x-ray diffraction intensities for characteristic reflections showing successive crystal structures as a function of temperature.

TABLE II. Comparison of the low-temperature crystal structures and reliability factors as obtained from synchrotron x-ray (SXRPD, $T = 10$ K) and neutron powder diffraction (NPD, $T = 15$ K).

	$\text{Pr}_{0.50}\text{Sr}_{0.40}\text{Ba}_{0.10}\text{CoO}_3$ 10 K (SXRPD) ^a	$\text{Pr}_{0.50}\text{Sr}_{0.50}\text{CoO}_3$ 15 K (NPD) ^b	$\text{Pr}_{0.50}\text{Sr}_{0.40}\text{Ca}_{0.10}\text{CoO}_3$ 10 K (SXRPD) ^a
Space group	<i>I4/mcm</i> (140)	<i>I4/mcm</i> (140)	<i>Imma</i> (74)
a (Å)	5.3732(1)	5.3585(1)	5.35768(3)
b (Å)	5.3732(1)	5.3585(1)	7.57005(4)
c (Å)	7.7053(1)	7.7093(1)	5.41025(3)
Vol (Å ³)	222.463(5)	221.367(9)	219.428(2)
Pr/Sr/A	4 <i>b</i>	4 <i>b</i>	4 <i>e</i>
x	0	0	0
y	0.5	0.5	0.25
z	0.25	0.25	-0.0014(2)
B (Å ²)	0.35(2)	0.790(6)	0.342(7)
Co	4 <i>c</i>	4 <i>c</i>	4 <i>b</i>
x	0	0	0
y	0	0	0
z	0	0	0.5
B (Å ²)	0.11(2)	0.459(2)	0.176(11)
O1	4 <i>a</i>	4 <i>a</i>	4 <i>e</i>
x	0	0	0
y	0	0	0.25
z	0.25	0.25	0.4444(9)
B (Å ²)	1.66(15)	1.190(1)	0.91(12)
O2	8 <i>h</i>	8 <i>h</i>	8 <i>g</i>
x	0.2205(8)	0.2849(3)	0.25
y	0.7205(8)	0.7849(3)	0.0242(7)
z	0	0	0.75
B (Å ²)	1.26(11)	1.028(6)	1.65(8)
χ^2	7.09	2.38	8.71
R_B (%)	4.26	2.39	4.79
R_{mag} (%)	–	7.2	–

^aMSPD; ^bD20 (Ref. [21]).

extending from ~ 127 K down to ~ 80 K, consistently with the anomalous step revealed by the magnetization (T_{SR}). In Fig. 7(b), we have plotted the temperature dependence of the coexisting orthorhombic and tetragonal structures during the O-T transformation. Table II reports the refined atomic coordinates refined for $\text{Pr}_{0.50}\text{Sr}_{0.40}\text{Ba}_{0.10}\text{CoO}_3$ at 10 K (*I4/mcm*). Figure 7(a) presents the Rietveld refinement plot corresponding to the tetragonal low-temperature phase (at 10 K). A small residual amount of untransformed phase [$\sim 9(1)\%$ wt.] was detected in the sample at low temperatures. The two structures are schematically represented in Fig. 7(c).

The *Imma* refined structure at 300 K is shown in Table III, which evidences that the O-R transition was already initiated at 300 K. At this temperature, a minor fraction of the *R-3c* phase was included to fit the SXRPD pattern ($\approx 9\%$ wt.). The beginning of the O-R transition at $T_{\text{OR}} \approx 300$ K upon heating is also suggested by the emerging visible changes close to RT, as shown in Fig. 6.

In addition, the evolution of the FM order was studied using the high-intensity, low-resolution powder diffractometer D1B ($\lambda = 2.52$ Å), well suited for magnetic order determination. A T - 2θ projection of the thermal evolution of the main

magnetic neutron-diffracted intensities is plotted in Fig. 8. Figure 9 shows the refinement of the neutron patterns collected at 285, 140, and 10 K for $\text{Pr}_{0.50}\text{Sr}_{0.40}\text{Ba}_{0.10}\text{CoO}_3$. At the two former temperatures, the compound follows the *Imma* symmetry, and below $T_C \approx 227$ K it adopts the *Im'm'a* FM order [magnetization parallel to x (referred to the tetragonal setting) and $1.406(3) \mu_B/\text{Co}$ at 140 K, Fig. 9(b)]. Below the SR transition at $T_{\text{SR}} \approx 80$ K, the *I4/mcm* structure was used for the neutron refinements using the *Fm'm'm* magnetic symmetry (FM1 phase) with $m_x = m_y$ [F_{xy} with $m_{\text{Co}} = 1.78(3) \mu_B/\text{Co}$ moments along the diagonal of the a - b plane]. The inset in Fig. 9(c) presents a schematic view of the low- T FM order. At 10 K, the magnetic moment reaches a value of $1.78(3) \mu_B/\text{Co}$, very similar to the moment found in PSCO ($m_{\text{Co}} = 1.87(4) \mu_B/\text{Co}$ [28]). The structural and magnetic details and reliability factors of the neutron refinements at 285, 140, and 10 K are listed in Table S1 (Supplemental Material [35]).

The FM ordering temperature T_C hardly varies with Ba content along the series. Here, T_C shows a tiny decrease by increasing Ba content ($T_C^{\text{onset}} \approx 238, 237, 231,$ and 227 K for $x = 0, 2.5, 5,$ and 10%), very likely due to the increase of

TABLE III. Crystal structures of $\text{Nd}_{0.50}\text{Sr}_{0.50}\text{CoO}_3$ as refined at 300 K (D2B) and at 400 K (D20; neutrons), and of $\text{Pr}_{0.50}\text{Sr}_{0.40}\text{Ba}_{0.10}\text{CoO}_3$ and $\text{Tb}_{0.50}\text{Sr}_{0.50}\text{CoO}_3$ at 300 K (synchrotron x-ray; MSPD).

	$\text{Pr}_{0.50}\text{Sr}_{0.40}\text{Ba}_{0.10}\text{CoO}_3$	$\text{Nd}_{0.50}\text{Sr}_{0.50}\text{CoO}_3$		$\text{Tb}_{0.50}\text{Sr}_{0.50}\text{CoO}_3$
	300 K	300 K	400 K	300 K
Space group	<i>Imma</i> (74)	<i>Imma</i> (74)	<i>R-3c</i> (167)	<i>Imma</i> (74)
a (Å)	5.4036(1)	5.3725(7)	5.4245(1)	5.36395(3)
b (Å)	7.6325(2)	7.6025(2)	5.4245(1)	7.58660(4)
c (Å)	5.4334(1)	5.4278(2)	13.1628(4)	5.36134(3)
Vol (Å ³)	224.086(8)	221.697(2)	335.425(2)	218.175(2)
Ln/Sr	4e	4e	6a	4e
x	0	0	0	0
y	0.25	0.25	0	0.25
z	0.0000(6)	0.0004(6)	0.25	-0.0002(7)
B (Å ²)	0.87(2)	0.791(5)	1.219(6)	1.21(1)
Co	4b	4b	6b	4b
x	0	0	0	0
y	0	0	0	0
z	0.5	0.5	0	0.5
B (Å ²)	0.49(3)	0.149(9)	0.724(5)	0.20(1)
O1	4e	4e	18e	4e
x	0	0	0.465(3)	0
y	0.25	0.25	0	0.25
z	0.4569(36)	0.4591(5)	0.25	0.4548(24)
B (Å ²)	4.7(4)	1.562(7)	1.567(5)	5.2(1)
O2	8g	8g	–	8g
x	0.25	0.25	–	0.25
y	0.0174(17)	0.0243(3)	–	0.0088(18)
z	0.75	0.75	–	0.75
B (Å ²)	1.79(19)	1.231(2)	–	5.2(1)
R_B (%)	5.52	3.58	3.32	5.95
R_f (%)	5.65	3.58	3.32	13.7
χ^2	9.22	1.67	2.76	5.54

the A-cation size variance (σ^2), as it occurs in similar FM perovskites displaying cation disorder [36,37]. Similarly, it is found that the variations observed in T_{OT} under the Sr/Ba substitution are less pronounced than in the Sr/Ca-substituted compounds.

B. Half-doped Sr-rich cobaltites without spontaneous SR

Magnetic measurements indicate that, by further decreasing the size of A-site cations, only one FM phase gets preserved in this family of half-doped cobaltites. Namely, the tetragonal phase and concurrent Co SR cease to occur, due to the stabilization of the *Imma* symmetry even at low temperatures (ground state). Thus, the magnetization and transport measurements reported by Yoshii and Abe [38] and Yosshii *et al.* [39] revealed a single FM transition (T_c) in $\text{Ln}_{0.50}\text{Sr}_{0.50}\text{CoO}_3$ perovskites for $Ln = \text{Nd, Sm, Eu, or Gd}$. These four distorted half-doped cobaltites are still metallic below RT despite their larger Co-O-Co distortions. A variety of SGs are found in the literature to describe these compounds due to the lack of more rigorous structural stud-

ies. For example, in Refs. [39,40], the XRD patterns for $\text{Ln}_{0.50}\text{Sr}_{0.50}\text{CoO}_3$ samples were assumed to be *Pnma* (for Nd and Sm) and *Pm-3m* (for Eu). In contrast, the x-ray diffraction data from $\text{Nd}_{0.50}\text{Sr}_{0.50}\text{CoO}_3$ were refined using the *Imma* SG in Ref. [41]. The *Pnma* symmetry was also attributed to the Nd-based compound in Refs. [38,42]. In Ref. [43], the *Pnma* symmetry was discarded for $\text{Eu}_{0.50}\text{Sr}_{0.50}\text{CoO}_3$. The structure of $\text{Tb}_{0.5}\text{Sr}_{0.5}\text{CoO}_3$ was refined by Srikiran and Yusuf [44] as *Pnma* for the whole temperature range <300 K.

In view of this dispersion of structural descriptions, next, we report a structural study of $\text{Nd}_{0.50}\text{Sr}_{0.50}\text{CoO}_3$ and the severely distorted $\text{Tb}_{0.5}\text{Sr}_{0.5}\text{CoO}_3$ cobaltite. Our analyses reveal that both present an *Imma* symmetry at RT.

I. $\text{Nd}_{0.50}\text{Sr}_{0.50}\text{CoO}_3$

Its magnetization and metallic resistivity below RT are plotted in Fig. 10. A drop in the magnetization curve was reported ~ 100 K when the magnetization is measured under moderate direct current (DC) fields ($H \geq \sim 1000$ Oe) [38]. This behavior is not related with the SR, and it comes from an antiferromagnetic alignment between $\text{Nd}(4f)$ and

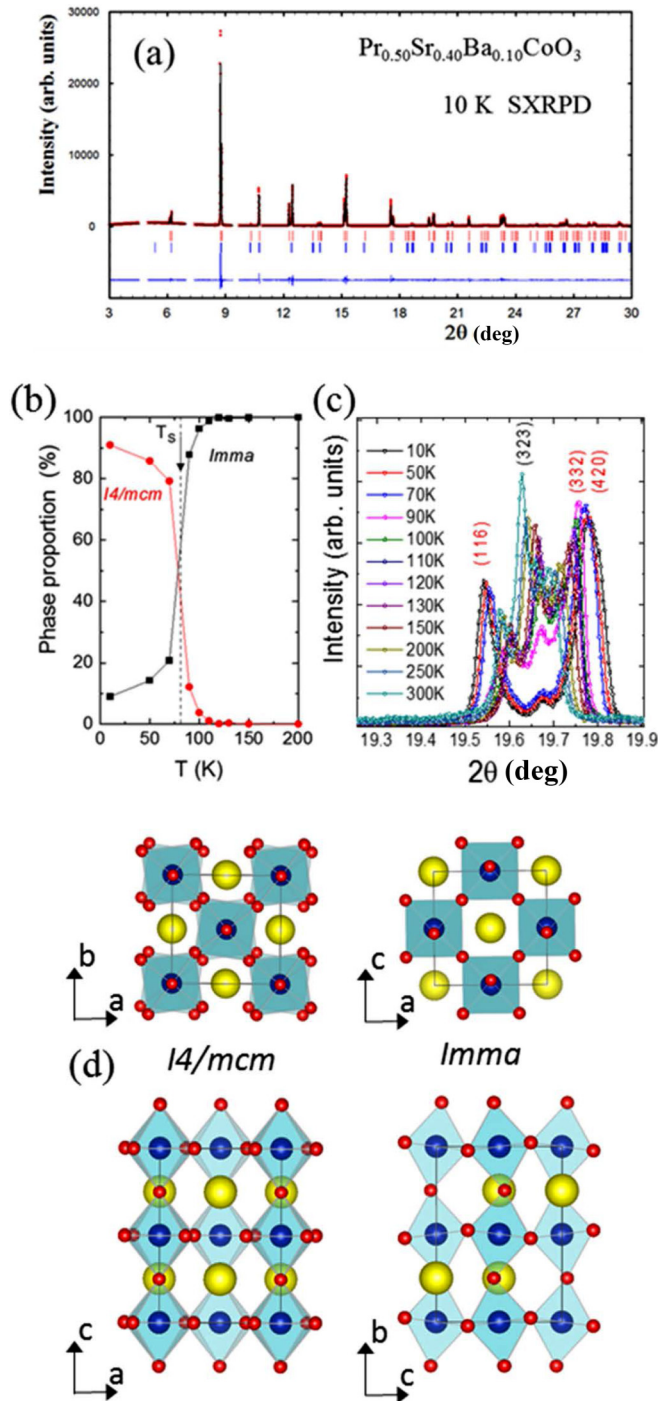


FIG. 7. $\text{Pr}_{0.50}\text{Sr}_{0.40}\text{Ba}_{0.10}\text{CoO}_3$: (a) Rietveld refinement of the synchrotron x-ray pattern at 10 K ($I4/mcm$, MSPD). (b) T evolution of the coexisting phase fractions across the low-temperature transition. (c) Synchrotron x-ray powder diffraction (SXRPD) as a function of temperature. A small residual amount of untransformed orthorhombic phase is present at 10 K [$\sim 9(1)\%$ wt. of the O phase is included in (a)]. (d) Projections of the $Imma$ and $I4/mcm$ structures.

$\text{Co}(3d)$ moments. Figure 11(b) plots the refinement of a high-resolution NPD pattern at 300 K on this Nd cobaltite (d2b@ill, $\lambda = 1.594 \text{ \AA}$). One can see that, unlike most of the earlier reports proposing a $Pnma$ structure, our high-resolution neu-

tron data is perfectly reproduced by the $Imma$ SG. After careful inspection, one can see that the reflections permitted by the $Pnma$ symmetry that are forbidden by the $Imma$ SG are not present in the neutron pattern. This is, for instance, the case of $h + k + l = 2n + 1$ or $h + l = 2n + 1$ type reflections, forbidden only under an $Imma$ cell (see Fig. S2 of the Supplemental Material [35]). Moreover, we have investigated the structural evolution of the $\text{Nd}_{0.50}\text{Sr}_{0.50}\text{CoO}_3$ cobaltite by neutron diffraction in the 10–410 K range (D20, $\lambda = 1.87 \text{ \AA}$). In Fig. 2(b), the thermal evolution of the neutron diffraction intensities discloses a single structural transition within this range ~ 340 K. Under heating conditions, this compound exhibits the $Imma \rightarrow R-3c$ transformation at $T_{\text{OR}} = 340$ K. As expected, T_{OR} is thus slightly higher than for PSCO, where it takes place at 314 K. In agreement with the evolution of the magnetization, the $Imma$ structure persists down to the lowest temperature, confirming that $\text{Nd}_{0.50}\text{Sr}_{0.50}\text{CoO}_3$ does not adopt the tetragonal ground state of $\text{Pr}_{0.50}\text{Sr}_{0.50}\text{CoO}_3$. The FM moment refined at 100 K was $1.58(5) \mu_B/\text{Co}$, with the same $Im'm'a$ MSG and orientation as the FM2 phase of PSCO (m_x , as referred to the $\sqrt{a_0} \times \sqrt{a_0} \times 2a_0$ cell). In Table III, we detail the structural parameters found for $\text{Nd}_{0.50}\text{Sr}_{0.50}\text{CoO}_3$ at 300 K ($Imma$) and at 400 K ($R-3c$).

2. $\text{Tb}_{0.50}\text{Sr}_{0.50}\text{CoO}_3$

The terbium-based cobaltite displays the most distorted unit cell among the $\text{Ln}_{0.50}\text{Sr}_{0.50}\text{CoO}_3$ compounds considered in this paper. Tb^{3+} is indeed smaller than Nd^{3+} , Sm^{3+} , Eu^{3+} , or Gd^{3+} . Figure 10(b) shows the magnetization and resistivity curves of the $\text{Tb}_{0.50}\text{Sr}_{0.50}\text{CoO}_3$ compound for $T < 300$ K. Despite the small ionic size of Tb^{3+} (1.095 \AA , IX coordination [45]), the $\text{Tb}_{0.50}\text{Sr}_{0.50}\text{CoO}_3$ solid solution is metallic with Curie temperature $T_C = 120$ K (see also Ref. [44]). Its magnetization indicates the absence of SR below the FM transition and therefore an orthorhombic ground state. The detailed structure of $\text{Tb}_{0.5}\text{Sr}_{0.5}\text{CoO}_3$ was reported by Srikan and Yusuf [44]—using NPD—as $Pnma$ in the whole temperature range for $T < 300$ K. In view of the present results, we have reexamined the structure of $\text{Tb}_{0.5}\text{Sr}_{0.5}\text{CoO}_3$ by means of synchrotron x-rays. A high-quality SXRPD pattern recorded on the MSPD beamline of the ALBA Synchrotron is shown in Fig. 12. Intensities were collected in the 4° – 55° angular interval using $\lambda = 0.424826 \text{ \AA}$. The suitability of both $Pnma$ and $Imma$ SGs was tested and compared. From the best fits using these two descriptions, we obtained the following agreement factors: (a) $R_B = 6.86\%$, $R_f = 16.0\%$, $R_p = 10.8\%$, $R_{wp} = 13.9\%$, and $\chi^2 = 4.05$ for $Pnma$; and (b) $R_B = 5.95\%$, $R_p = 10.8\%$, $R_{wp} = 13.6\%$, $R_f = 13.7\%$, and $\chi^2 = 5.54$ for $Imma$. The $Imma$ refined pattern is shown in Fig. 12. In Fig. S3 (Supplemental Material [35]), we compare a selected interval of the two refinements with the focus in the low-intensity scale. Several extremely low-intensity and very wide reflections were detected in the SXRPD pattern that are characteristic of the $Pnma$ symmetry ($\{023\}$, $\{131\}$, $\{115\}$, etc.). They are noticeably less intense (~ 200 times) and far wider than $Imma$ reflections (see Fig. S3, Supplemental Material [35]). Consequently, the structure of $\text{Tb}_{0.5}\text{Sr}_{0.5}\text{CoO}_3$ should be regarded as $Imma$, ruling out a $Pnma$ -type distortion, even though very minority short-range

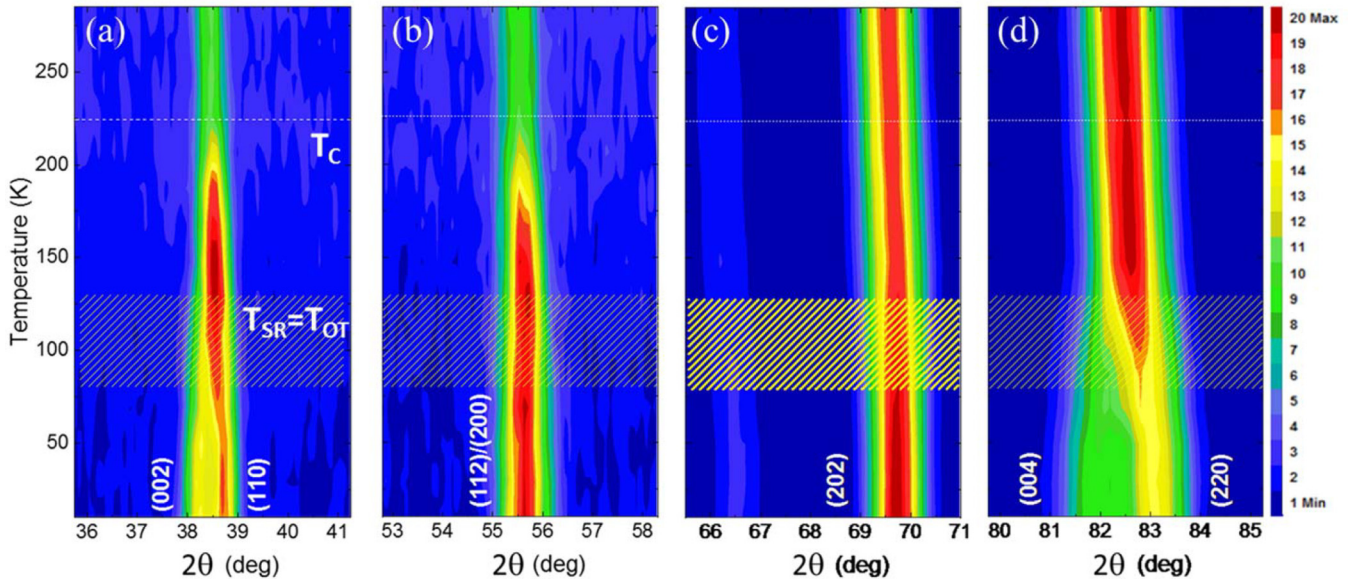


FIG. 8. $\text{Pr}_{0.50}\text{Sr}_{0.40}\text{Ba}_{0.10}\text{CoO}_3$: T - 2θ projection of the T dependence for the neutron-diffracted intensities around selected reflections. Changes are evident at T_c and $T_{\text{SR}} = T_{\text{OT}}$ (symmetry and spin-rotation transition, D1B).

$Pnma$ distortions may exist (perhaps related to defects favored by the cation-size mismatch). The refined $Imma$ structure of

$\text{Tb}_{0.5}\text{Sr}_{0.5}\text{CoO}_3$ is reported in Table III. Disorder effects due to the high cation-size mismatch in this solid solution appear in the form of large values for some refined thermal factors.

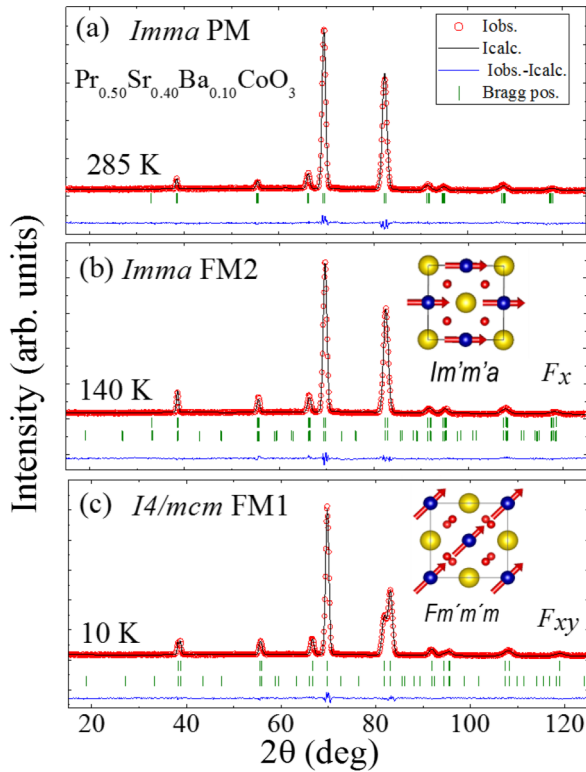


FIG. 9. $\text{Pr}_{0.50}\text{Sr}_{0.40}\text{Ba}_{0.10}\text{CoO}_3$: Rietveld refinement (black line) of the neutron patterns (D1B) obtained at (a) 285 K [$Imma$ SG], (b) 140 K [$Im'm'a$ magnetic SG (MSG)] and (c) 10 K ($Fm'm'm$ MSG). The second row of Bragg positions is the magnetic phase. A projection of the magnetic structures is also shown (yellow balls are Pr/Ba/Sr atoms in yellow, Co atoms in blue, and O atoms in red).

3. $\text{Gd}_{0.5}\text{Sr}_{0.5}\text{CoO}_3$

Although the $\text{Gd}_{0.5}\text{Sr}_{0.5}\text{CoO}_3$ unit cell structure was refined using $Pnma$ symmetry from laboratory x-ray data in Ref. [46], the size of Gd lies in between Nd and Tb ($\langle r_0 \rangle$: 1.163 Å [Nd^{3+}] > 1.107 Å [Gd^{3+}] > 1.095 Å [Tb^{3+}]). As we have shown in the precedent paragraphs, both the Nd and Tb half-doped cobaltites order with $Imma$ symmetry below RT, and therefore, the Gd-based compound should also be considered to display the same symmetry.

C. Phase diagram

After the characterization and the results reported in the precedent sections, we have elaborated the $\langle r_A \rangle$ - T phase diagram of the half-doped Sr-rich $\text{Ln}_{0.50}(\text{Sr}, \text{A})_{0.50}\text{CoO}_3$ cobaltites shown in Fig. 13. The different regions in the phase diagram correspond to: (i) paramagnetic $R-3c$ ($a^-a^-a^-$ distortion in Glazer notation); (ii) paramagnetic $Imma$ [$a^-a^-c^0$ in the $Ibmm$ setting ($\sqrt{2}a_0 \times \sqrt{2}a_0 \times 2a_0$), the setting used for the tetragonal cell]; (iii) $Im'm'a = F_x$ FM (FM2) $Imma$ phase; and (iv) $Fm'm'm = F_{xy}$ FM (FM1) $I4/mcm$ phase ($a^0a^0c^-$).

The full numerical information gathered in Fig. 13 is also listed in Table S2 (Supplemental Material [35]). Here, T_{RO} temperatures are represented by green triangles ($R-3c \rightarrow Imma$), the Curie temperatures T_c are represented by black squares/circles (PM \rightarrow FM1), and $T_{\text{SR}} (=T_{\text{OT}}$, onset) is represented by red rhombi (FM1/ $Imma \rightarrow$ FM2/ $I4/mcm$). White and red rhombi indicate the middle point of the transition in the magnetization measurements. Black circles correspond to T_c values for $\text{Ln}_{0.50}\text{Sr}_{0.50}\text{CoO}_3$ ($\text{Ln} = \text{Sm}, \text{Eu}, \text{or Gd}$, extracted respectively from Refs. [38,47,48]).

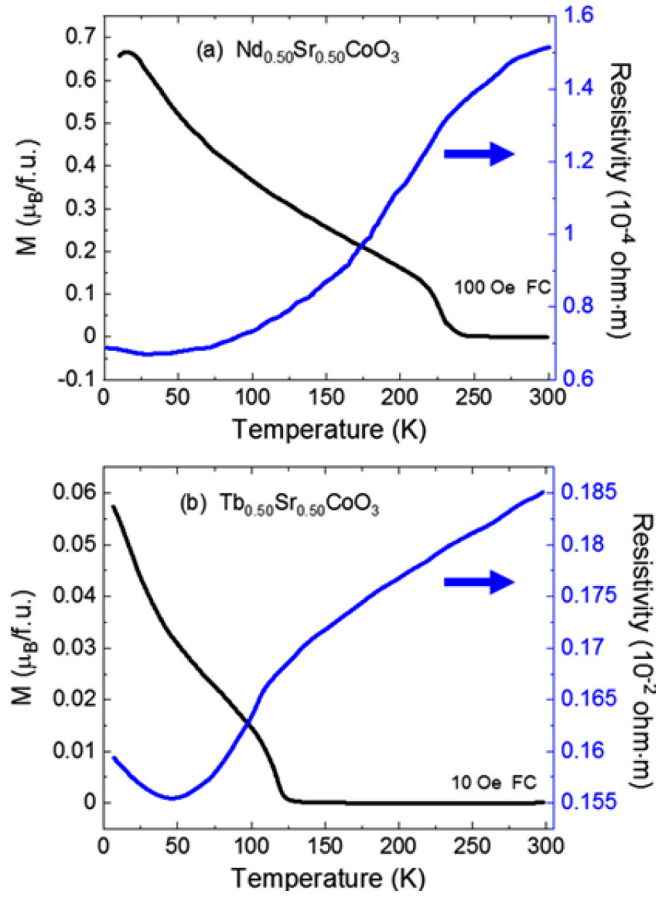


FIG. 10. Field cooling (FC) magnetization curves and resistivity of (a) $\text{Nd}_{0.50}\text{Sr}_{0.50}\text{CoO}_3$ and (b) $\text{Tb}_{0.50}\text{Sr}_{0.50}\text{CoO}_3$.

First, despite distinct SGs were formerly used to describe the orthorhombic phases of $\text{Ln}_{0.50}\text{Sr}_{0.50}\text{CoO}_3$ compounds, Fig. 13 unveils that the orthorhombic structures are always $Imma$, at least down to $\text{Ln} = \text{Tb}$. Therefore, the rhombohedral-to-orthorhombic transition is of the $R-3c \rightarrow Imma$ type. Thus, none of the compounds studied showed $Pnma$ symmetry. More interestingly, there is a $T-(r_A)$ confined region in the phase diagram of these Sr-rich half-doped cobaltites where the ground state exhibits a tetragonal $I4/mcm$ structure and presents F_{xy} magnetization from cobalt, yielding an overall $Fm'm'm$ symmetry. This region has been determined, and it is shown in Fig. 13. The borderline between this region and the $Im'm'a$ phase identifies the $T_{SR}((r_A))$ line in the phase diagram where the spontaneous SR takes place. The reorientation of the easy axis of cobalt follows the suppression of the orthorhombic tilting of the octahedra in antiphase along a and b pseudocubic axes ($a^-a^-c^0 \rightarrow a^0a^0c^-$). The small tilting around the vertical axis that occurs in antiphase for successive octahedra along c is an additional distortion that does not play a main active role for the SR. The stability region of the $Fm'm'm$ tetragonal magnetic phase vanishes for structural distortions very close to $\text{Nd}_{0.50}\text{Sr}_{0.50}\text{CoO}_3$. We found that the SR is suppressed in this cobaltite, which already presents an orthorhombic metallic ground state.

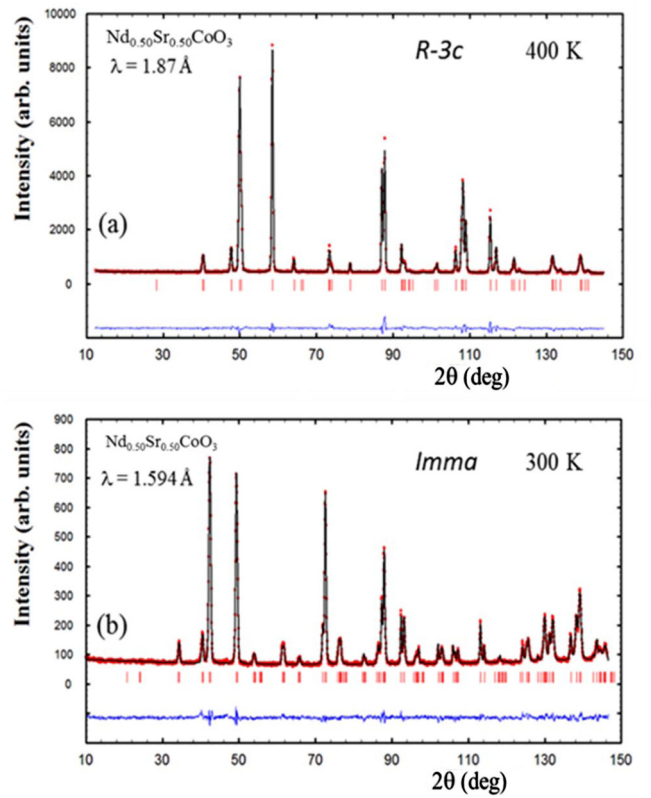


FIG. 11. $\text{Nd}_{0.50}\text{Sr}_{0.50}\text{CoO}_3$: Rietveld refinements (black line) of the neutron patterns at (a) 400 K, $R-3c$ (D20) and (b) 300 K, $Imma$ (D2B; red circles, experimental points; bottom blue line, difference).

IV. CONCLUSIONS

The $\text{Pr}_{0.50}\text{Sr}_{0.50}\text{CoO}_3$ perovskite exhibits unique magnetostructural properties among the rest of FM/metallic $\text{Ln}_{0.50}\text{Sr}_{0.50}\text{CoO}_3$ compounds. They are triggered by the transformation of an orthorhombic $Imma$ structure into a tetragonal $I4/mcm$ symmetry.

Summarizing, the stability of the ground FM/metallic tetragonal structure (MSG $Fm'm'm$) has been investigated

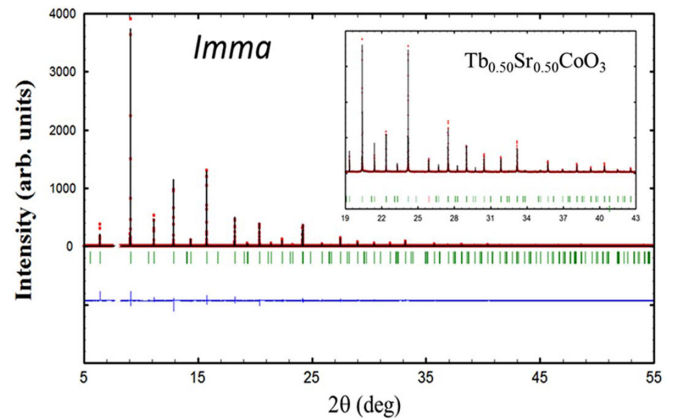


FIG. 12. $\text{Tb}_{0.50}\text{Sr}_{0.50}\text{CoO}_3$: Rietveld refinement (black line) of the synchrotron x-ray pattern at 300 K using the $Imma$ space group (MSPD; red circles, experimental points; bottom blue line, difference). Inset: Detail of the 10° – 30° interval.

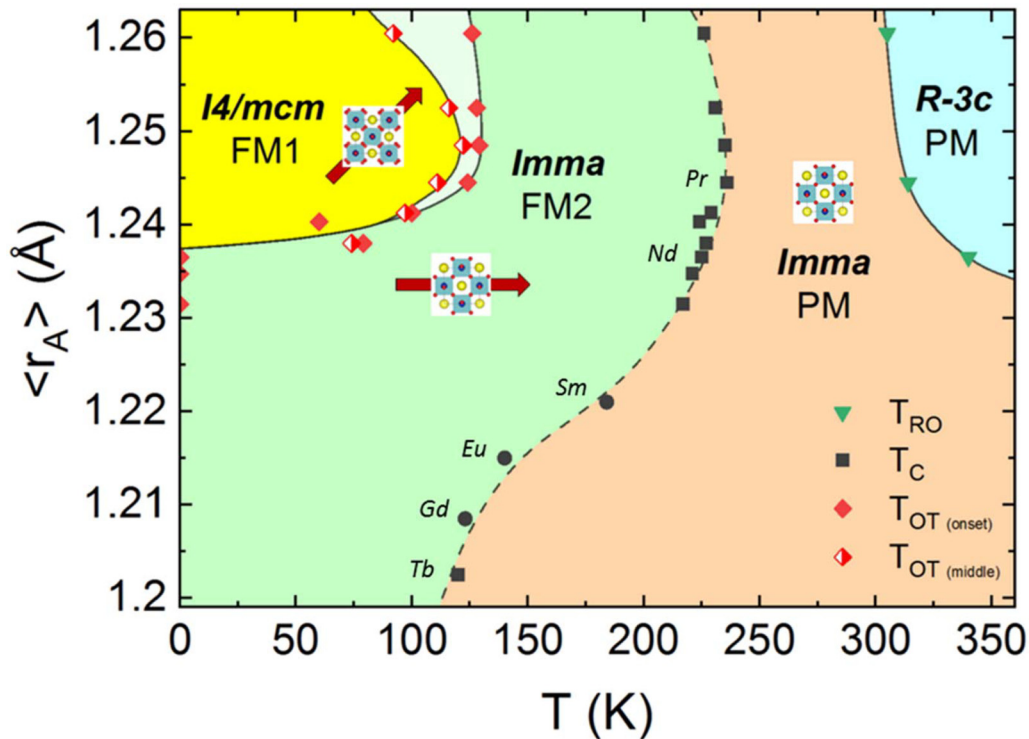


FIG. 13. $\langle r_A \rangle$ - T phase diagram of the half-doped Sr-rich $Ln_{0.50}(Sr, A)_{0.50}CoO_3$ cobaltites ($A = Ba$ or Ca). T_{RO} are represented by green triangles ($R-3c \rightarrow Imma$), the Curie temperatures T_C are represented by black squares/circles (PM \rightarrow FM1) and red rhombuses represent $T_{OT} = T_{SR}$ (FM1/ $Imma \rightarrow$ FM2/ $I4/mcm$). Black circles correspond to T_C values for $Ln_{0.50}Sr_{0.50}CoO_3$ ($Ln = Sm, Eu,$ or Gd) as extracted from Refs. [37,46,47]. The easy axis in FM1 and FM2 phases are indicated.

in bigger and smaller cells, partially substituting Sr^{2+} with bigger (Ba^{2+}) and smaller (Ca^{2+}) alkaline-earth ions. In addition, Pr^{3+} ions were substituted with other lanthanides. Their structural and magnetic properties were characterized by synchrotron, NPD, and magnetometry. As a result, we have built a T - $\langle r_A \rangle$ phase diagram for half-doped $Ln_{0.50}(Sr_{1-x}A_x)_{0.50}CoO_3$ cobaltites <360 K as a function of temperature and the distortion of the perovskite structures. We have identified the stability region where a tetragonal $Fm'm'm$ metallic phase, with the magnetization direction rotated by 45° within the a - b plane, replaces the orthorhombic $Im'm'a$ phase with F_x FM moments. The limits of this region have been determined, and its boundaries draw the line where a spontaneous SR of Co moments takes place.

ACKNOWLEDGMENTS

We acknowledge financial support from the Spanish Ministerio de Ciencia, Innovación y Universidades (MIN-CIU), through Projects No. RTI2018-098537-B-C21 and No. RTI2018-098537-B-C22, cofunded by ERDF from the EU, and “Severo Ochoa” Programme for Centres of Excellence in R&D [FUNFUTURE (CEX2019-000917-S)]. X.Z. was financially supported by China Scholarship Council (CSC) with No. 201706080017. A.R. and X.Z.’s work was done as a part of the Ph.D. program in Materials Science at Universitat Autònoma de Barcelona. We also acknowledge ALBA (2014071047, 2015091512), ILL, and D1B-CRG (MINCIU) for provision of beam time (CRG-D1B-14-293, CRG-2149-142, 5-31-1963).

- [1] W. Kobayashi, S. Ishiwata, I. Terasaki, M. Takano, I. Grigoraviciute, H. Yamauchi, and M. Karppinen, *Phys. Rev. B* **72**, 104408 (2005).
- [2] Z. Shao and S. M. Haile, in *Materials for Sustainable Energy: A Collection of Peer-Reviewed Research and Review Articles from Nature Publishing Group*, edited by V. Dusastre (Nature Publishing Group, London, 2010), p. 255.
- [3] Y. Wang, N. S. Rogado, R. J. Cava, and N. P. Ong, *Nature* **423**, 425 (2003).
- [4] K. Takada, H. Sakurai, E. Takayama-Muromachi, F. Izumi, R. A. Dilanian, and T. Sasaki, *Nature* **422**, 53 (2003).
- [5] Z. Fang, L. Chen, Y. Ni, C. Lu, and Z. Xu, *Appl. Surf. Sci.* **469**, 76 (2019).
- [6] B. Raveau and M. Seikh, *Cobalt Oxides: From Crystal Chemistry to Physics* (Wiley-VCH Verlag GmbH & Co. KGaA, 2012).
- [7] S. Tsubouchi, T. Kyômen, M. Itoh, P. Ganguly, M. Oguni, Y. Shimojo, Y. Morii, and Y. Ishii, *Phys. Rev. B* **66**, 052418 (2002).

- [8] C. Frontera, J. L. García-Muñoz, A. Llobet, M. A. G. Aranda, J. Rodríguez-Carvajal, M. Respaud, J. M. Broto, B. Raquet, H. Rakoto, and M. Goiran, *J. Magn. Magn. Mater.* **242–245**, 751 (2002).
- [9] C. Frontera, J. L. García-Muñoz, A. Llobet, L. Mañosa, and M. A. G. Aranda, *J. Solid State Chem.* **171**, 349 (2003).
- [10] A. Maignan, V. Caignaert, B. Raveau, D. Khomskii, and G. Sawatzky, *Phys. Rev. Lett.* **93**, 026401 (2004).
- [11] M. Medarde, C. Dallera, M. Grioni, J. Voigt, A. Podlesnyak, E. Pomjakushina, K. Conder, Th. Neisius, O. Tjernberg, and S. N. Barilo, *Phys. Rev. B* **73**, 054424 (2006).
- [12] M. Motin Seikh, V. Pralong, O. I. Lebedev, V. Caignaert, and B. Raveau, *J. Appl. Phys.* **114**, 013902 (2013).
- [13] A. J. Barón-González, C. Frontera, J. L. García-Muñoz, J. Blasco, and C. Ritter, *Phys. Rev. B* **81**, 054427 (2010).
- [14] K. Knížek, J. Hejtmánek, P. Novák, and Z. Jirák, *Phys. Rev. B* **81**, 155113 (2010).
- [15] J. L. García-Muñoz, C. Frontera, A. J. Barón-González, S. Valencia, J. Blasco, R. Feyerherm, E. Dudzik, R. Abrudan, and F. Radu, *Phys. Rev. B* **84**, 045104 (2011).
- [16] J. Herrero-Martín, J. L. García-Muñoz, S. Valencia, C. Frontera, J. Blasco, A. J. Barón-González, G. Subías, R. Abrudan, F. Radu, E. Dudzik, and R. Feyerherm, *Phys. Rev. B* **84**, 115131 (2011).
- [17] Y. Okimoto, X. Peng, M. Tamura, T. Morita, K. Onda, T. Ishikawa, S. Y. Koshihara, N. Todoroki, T. Kyomen, and M. Itoh, *J. Phys.: Conf. Ser.* **148**, 012019 (2009).
- [18] Y. Kanamori, H. Matsueda, and S. Ishihara, *Phys. Rev. Lett.* **107**, 167403 (2011).
- [19] W. Koshibae, N. Furukawa, and N. Nagaosa, *Phys. Rev. B* **87**, 165126 (2013).
- [20] S. G. Zhao, A. Gu, X. L. Yan, L. M. Hao, Y. Xie, T. Zhang, and K. X. Jin, *Europhys. Lett.* **108**, 67007 (2014).
- [21] J. Padilla-Pantoja, J. L. García-Muñoz, B. Bozzo, Z. Jirák, and J. Herrero-Martín, *Inorg. Chem.* **53**, 12297 (2014).
- [22] J. Padilla-Pantoja, J. L. García-Muñoz, B. Bozzo, Z. Jirák, and J. Herrero-Martín, *Inorg. Chem.* **54**, 6062 (2015).
- [23] J. Padilla-Pantoja, J. Herrero-Martín, P. Gargiani, S. M. Valvidares, V. Cuartero, K. Kummer, O. Watson, N. B. Brookes, and J. L. García-Muñoz, *Inorg. Chem.* **53**, 8854 (2014).
- [24] R. Mahendiran and P. Schiffer, *Phys. Rev. B* **68**, 024427 (2003).
- [25] M. Uchida, R. Mahendiran, Y. Tomioka, Y. Matsui, K. Ishizuka, and Y. Tokura, *Appl. Phys. Lett.* **86**, 131913 (2005).
- [26] J. Padilla-Pantoja, J. Herrero-Martín, E. Pellegrin, P. Gargiani, S. M. Valvidares, A. Barla, and J. L. García-Muñoz, *Phys. Rev. B* **92**, 245136 (2015).
- [27] J. Padilla-Pantoja, J. Herrero-Martín, E. Pellegrin, P. Gargiani, S. M. Valvidares, A. Barla, and J. L. García-Muñoz, *Phys. Rev. B* **93**, 039903(E) (2016).
- [28] J. L. García-Muñoz, J. Padilla-Pantoja, X. Torrelles, J. Blasco, J. Herrero-Martín, B. Bozzo, and J. A. Rodríguez-Velamazán, *Phys. Rev. B* **94**, 014411 (2016).
- [29] J. Grollier, D. Querlioz, K. Y. Camsari, K. Everschor-Sitte, S. Fukami, and M. D. Stiles, *Nat. Electron.* **3**, 360 (2020).
- [30] N. Locatelli, V. Cros, and J. Grollier, *Nat. Mater.* **13**, 11 (2014).
- [31] R. V. Mikhaylovskiy, E. Hendry, A. Secchi, J. H. Mentink, M. Eckstein, A. Wu, R. V. Pisarev, V. V. Kruglyak, M. I. Katsnelson, T. Rasing, and A. V. Kimel, *Nat. Commun.* **6**, 8190 (2015).
- [32] F. Fauth, R. Boer, F. Gil-Ortiz, C. Popescu, O. Vallcorba, I. Peral, D. Fullà, J. Benach, and J. Juanhuix, *Eur. Phys. J. Plus* **130**, 160 (2015).
- [33] J. Rodríguez-Carvajal, *Physica B* **192**, 55 (1993).
- [34] P. M. Woodward, *Acta Cryst.* **53**, 32 (1997).
- [35] See Supplemental Material at <http://link.aps.org/supplemental/10.1103/PhysRevB.104.054411> for details about magnetic hysteresis $M(H)$ cycles; comparison of Rietveld fits ($Imma$ vs $Pnma$) for $Ln_{0.5}Sr_{0.5}CoO_3$ ($Ln = Nd$ and Tb); neutron diffraction results for $Pr_{0.50}Sr_{0.40}Ba_{0.10}CoO_3$ at 10, 140, and 285 K; and the list of structural and magnetic transition temperatures for $Ln_{0.50}(Sr, A)_{0.50}CoO_3$ compounds ($A = Ba, Ca$).
- [36] L. M. Rodríguez-Martínez and J. P. Attfield, *Phys. Rev. B* **54**, R15622 (1996).
- [37] J. A. Collado, C. Frontera, J. L. García-Muñoz, and M. A. G. Aranda, *J. Solid State Chem.* **178**, 1949 (2005).
- [38] K. Yoshii and H. Abe, *Phys. Rev. B* **67**, 094408 (2003).
- [39] K. Yoshii, H. Abe, and A. Nakamura, *Mater. Res. Bull.* **36**, 1447 (2001).
- [40] A. Mineshige, M. Inaba, T. Yao, and Z. Ogumi, *J. Solid State Chem.* **121**, 423 (1996).
- [41] S. Kundu and T. K. Nath, *J. Phys.: Condens. Matter* **24**, 236005 (2012).
- [42] P. Kumar and R. Mahendiran, *Appl. Phys. Lett.* **101**, 042411 (2012).
- [43] R. Li, F. Li, J. Fang, W. Tong, C. Zhang, L. Pi, and Y. Zhang, *J. Alloys Compd.* **577**, 303 (2013).
- [44] J. S. Srikanan and S. M. Yusuf, *J. Alloys Compd.* **390**, 26 (2005).
- [45] R. D. Shannon, *Acta Cryst.* **32**, 751 (1976).
- [46] P. V. Vanitha, A. Arulraj, P. N. Santhosh, and C. N. R. Rao, *Chem. Mater.* **12**, 1666 (2000).
- [47] M. Zhuang, W. Zhang, and N. Ming, *Phys. Rev. B* **57**, 10705 (1998).
- [48] F. Li and J. Fang, *J. Magn. Magn. Mater.* **324**, 2664 (2012).